Proceedings of the ASME 2012 International Design Engineering Technical Conferences & Computers and Information in Engineering Conference
IDETC/CIE 2012
August 12-15, 2012, Chicago, IL, USA

DETC2012-70648

ON THE NONLINEAR DYNAMICS OF ELECTROMAGNETICALLY-TRANSDUCED MICRORESONATORS

Andrew B. Sabater, Vijay Kumar, Aamer Mahmood, Jeffrey F. Rhoads*
School of Mechanical Engineering,
Birck Nanotechnology Center,
and Ray W. Herrick Laboratories
Purdue University
West Lafayette, Indiana 47907
Email: jfrhoads@purdue.edu

ABSTRACT

This work investigates the dynamics of electromagnetically-actuated and sensed microresonators. These resonators consist of a silicon microcantilever and a current-carrying metallic wire loop. When placed in a permanent magnetic field, the devices vibrate due to Lorentz interactions. These vibrations, in turn, induce an electromotive force, which can be correlated to the dynamic response of the device. The nature of this transduction process results in an intrinsic coupling between the system's input and output, which must be analytically and experimentally characterized to fully understand the dynamics of the devices of interest. This paper seeks to address this need through the modeling, analysis, and experimental characterization of the nonlinear response of electromagnetically-transduced microcantilevers in the presence of inductive and resistive coupling between the devices' input and output ports. A complete understanding of this behavior should enable the application of electromagnetically-transduced microsystems in practical contexts ranging from resonant mass sensing to micromechanical signal processing.

1 INTRODUCTION

Over the past two decades, resonant MEMS devices have become an integral part of numerous technologies in the transportation, health, consumer electronics, and defense sectors. While MEMS devices can be actuated and sensed through a wide variety of mechanisms, this paper focuses on electromagnetic (also known as magnetomotive) transduction. In microscale contexts, electromagnetic transduction is appealing, because it offers the benefits of scalability, self-sensing and near-seamless integration with external electronics and associated hardware elements. These advantages render electromagnetically-transduced microresonators suitable for a variety of applications, including mass sensing and micromechanical signal processing [1–8].

A majority of the electromagnetically-actuated devices introduced to date consist of a compliant structural resonator with a current-carrying wire loop affixed to its surface (in some cases, the resonator itself acts as the current-carrying conductor). When placed in an external magnetic field, the flow of current through the wire loop induces a Lorentz force on the resonator, which results in mechanical motion. The movement of the current-carrying conductor through the external magnetic field, in turn, results in an induced electromotive force (EMF), which can be utilized for sensing purposes.

The microresonator detailed herein is similar in form to those previously introduced in [9–13]. The system consists of an electrically- and mechanically-isolated silicon microcantilever, which has two current loops (one for actuation and one for sensing) affixed to its surface. While this simplicity in physical design allows for high-yield device fabrication, the electromagnetic transduction approach introduces some complexity into

*Address all correspondence to this author.

the design and development process, due to the intrinsic coupling which exists between the input and output ports of the device. To minimize these coupling effects and achieve frequency separation between the input and output signals, many of the works detailed above exploited the dynamic behaviors of electromagnetically-transduced devices which were parametrically excited [9–12]. In order to utilize such devices under direct excitation, the coupling between the input and output ports must be fully characterized. While input/output coupling mechanisms akin to that investigated here have been previously considered within the context of carbon nanotube and piezoelectric crystal resonators (see, for example, [14, 15]), the present work seeks to characterize the impact of this mechanism on the dynamic response of electromagnetically-transduced microresonators.

The paper begins in Section 2 with the modeling, and subsequent analysis, of the dynamic response of the electromagnetically-transduced microresonators of interest, building, in part, upon the results of [16]. The work then continues in Section 3 with the development, and subsequent analysis, of a model for the microresonators' induced EMF in the presence of coupling between the devices' input and output ports, due to both resistive and inductive sources. Section 4 briefly describes the design and fabrication processes utilized for the electromagnetically-transduced microresonators, and then proceeds with the experimental characterization of a representative device. Ultimately, the paper concludes with a brief summary and a discussion of current and future research directions.

2 THE DYNAMICS OF AN ELECTROMAGNETICALLY-ACTUATED MICROBEAM

As previously noted and highlighted in Fig. 1, the devices of interest consist of an electrically- and mechanically-isolated microcantilever with two integrated Au/Cr wire loops, which is placed in a permanent magnetic field. To differentiate between the two wire loops in Fig. 1, the outer wire loop has been colored yellow and the inner loop has been colored red. Note that the magnetic field is oriented at an angle α with respect to the vertical reference (Fig. 2), and, due to the scale of the device and the permanent magnet that is employed, the magnitude and direction of the field are assumed to be constants.

Assuming that the beam has a negligible rotational inertia, the specific Lagrangian $\bar{L}$ of the device is defined as

$$\bar{L} = \frac{1}{2}\rho A\left[\dot{u}^2 + \dot{v}^2\right] - \frac{1}{2}EI\psi'^2, \tag{1}$$

where $(\dot{\bullet})$ and $(\bullet)'$ denote the derivatives with respect to time and the arc length variable s, respectively, and u, v and ψ are defined as in Fig. 3. Note that ρ is the mass density of the microbeam,

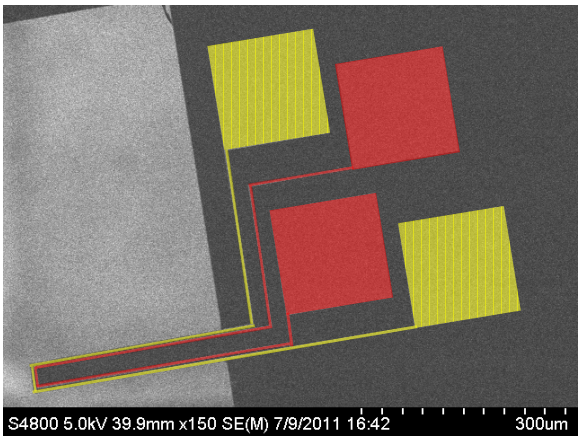

(a)

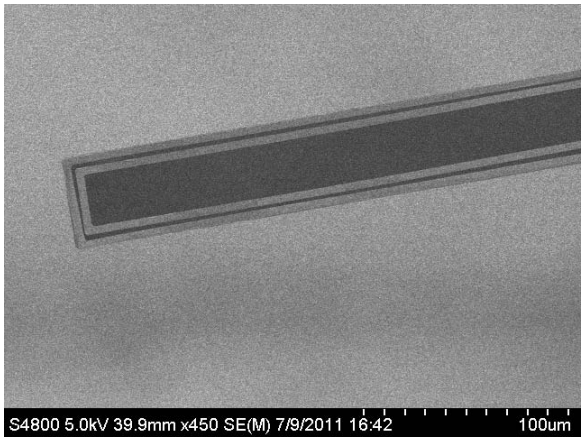

(b)

FIGURE 1. SCANNING ELECTRON MICROGRAPH OF A REPRESENTATIVE ELECTROMAGNETICALLY-TRANSDUCED MICRORESONATOR. AS SHOWN IN (a), THE DEVICE CONSISTS OF AN ELECTRICALLY- AND MECHANICALLY-ISOLATED SILICON MICROCANTILEVER AND TWO Au/Cr WIRE LOOPS, WHICH FOLLOW THE PERIMETER OF THE MICROCANTILEVER. THE TWO WIRE LOOPS ARE SHOWN IN DETAIL IN (b).

A is the cross-sectional area, l is the undeformed length, g is the width, E is the modulus of elasticity and I is the cross-sectional moment of inertia.

The application of extended Hamilton's principle results in the following variational equation of motion for the system:

$$\begin{aligned}\delta H =& 0\\ =& \delta\int_{t_1}^{t_2}\int_0^l \left\{\bar{L} + \frac{1}{2}\lambda\left[1-(1+u')^2-(v')^2\right]\right\}\mathrm{d}s\mathrm{d}t\\ &+ \int_{t_1}^{t_2}\int_0^l (Q_u\delta u + Q_v\delta v)\mathrm{d}s\mathrm{d}t,\end{aligned} \tag{2}$$

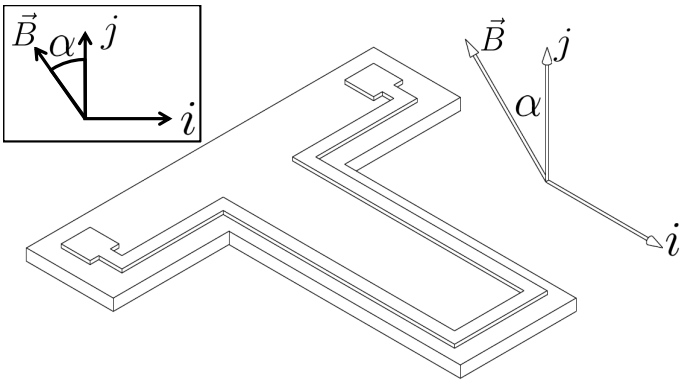

FIGURE 2. SCHEMATIC DIAGRAM OF THE BEAM IN THREE DIMENSIONS. AS SHOWN IN THE INSET, THE MAGNETIC FIELD $\vec{B}$ IS ORIENTED AT AN ANGLE α WITH RESPECT TO THE VERTICAL REFERENCE. NOTE THAT ONLY ONE OF THE TWO WIRE LOOPS IS DEPICTED.

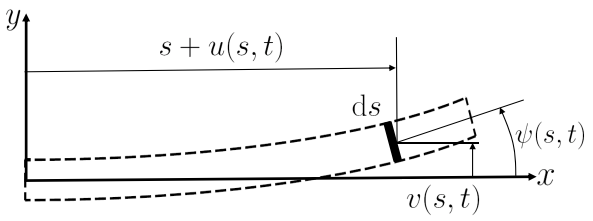

FIGURE 3. SCHEMATIC DIAGRAM OF THE BEAM ELEMENT AND DYNAMIC VARIABLES USED FOR MODELING. NOTE THAT u, v AND ψ ARE THE LONGITUDINAL, TRANSVERSE AND ANGULAR DISPLACEMENTS OF THE DIFFERENTIAL BEAM ELEMENT, RESPECTIVELY, AND s IS THE ARC LENGTH VARIABLE.

where λ is a Lagrange multiplier used to enforce an inextensibility constraint and Q_u and Q_v are the nonconservative forces in the longitudinal and transverse directions, respectively. The nonconservative forces are assumed to be point loads applied to the tip of the beam and capture longitudinal and transverse components of the Lorentz force, as well as an additional force contribution in the transverse direction attributable to viscous damping. Note that c represents the specific viscous damping coefficient.

Integrating Eqn. (2) successively by parts yields the two equations that govern the longitudinal and transverse vibrations of the system. Utilizing third-order Taylor's series expansions for u and ψ, an approximate solution for the Lagrange multiplier λ can be found, and subsequently used to reduce the two equations to a single equation which governs the transverse vibrations of the system. Nondimensionalizing the variables in the model, such that

$$\hat{v} = \frac{v}{v_0}, \quad \hat{s} = \frac{s}{l}, \quad \hat{t} = \frac{t}{T}, \tag{3}$$

where v_0 is the beam's thickness, and

$$T = \sqrt{\frac{\rho A l^4}{EI}}, \quad \hat{c} = \frac{cT}{\rho A}, \tag{4}$$

yields a distributed-parameter model for the system. To study the dynamics of the system near the primary resonance, the distributed parameter model can be reduced to an ordinary differential equation via modal projection. Introducing a single-mode expansion of the form

$$\hat{v}(\hat{s},\hat{t}) = z(\hat{t})\Psi(\hat{s}), \tag{5}$$

where Ψ is the first mode shape of an ideal cantilever and z is the displacement in the first mode, projecting the result onto the first mode shape, and rescaling the time variable (again) yields the final lumped-parameter equation of motion for the system:

$$\begin{aligned} z'' + \frac{\varepsilon}{Q} z' + [1 + \varepsilon\lambda_1 i(\tau)]\, z + [\varepsilon k_3 + \varepsilon\lambda_3 i(\tau)]\, z^3 \\ + \varepsilon\beta(z z'^2 + z^2 z'') = \varepsilon\eta_1 i(\tau). \end{aligned} \tag{6}$$

Here, Q represents the resonator's quality factor, $i(\tau)$ is the excitation current, and ε is a bookkeeping parameter introduced to facilitate analysis. The remainder of the parameters included here are defined in Table 1.

Assuming all parameters with an ε scaling in Eqn. (6) are sufficiently small, the method of averaging can be used to generate the frequency response of the resonator. Employing the following coordinate transformation,

$$\begin{aligned} z(\tau) &= a(\tau)\cos[\tau + \phi(\tau)], \\ z'(\tau) &= -a(\tau)\sin[\tau + \phi(\tau)], \end{aligned} \tag{7}$$

assuming that the excitation current is at a single frequency Ω,

$$i(\tau) = i_0 \cos\Omega\tau, \tag{8}$$

and introducing a detuning parameter to characterize the difference between the natural frequency of the microbeam and the excitation frequency,

$$\varepsilon\sigma = \Omega - 1, \tag{9}$$

TABLE 1. DEFINITIONS OF THE NONDIMENSIONAL PARAMETERS USED IN EQN. (6).

$$\omega_0^2 = \int_0^1 \Psi\Psi^{iv}\mathrm{d}\hat{s}$$

$$\tau = \omega_0 \hat{t}$$

$$(\bullet)' = \frac{\partial(\bullet)}{\partial\tau}$$

$$\varepsilon k_3 = \frac{v_0^2}{l^2\omega_0^2}\left(4\int_0^1 \Psi\Psi'\Psi''\Psi'''\mathrm{d}\hat{s} + \int_0^1 \Psi\Psi''^3\mathrm{d}\hat{s} + \int_0^1 \Psi\Psi'^2\Psi^{iv}\mathrm{d}\hat{s}\right)$$

$$\varepsilon\lambda_1 = \frac{gBl^2\cos\alpha}{EI\omega_0^2}\int_0^1 \Psi'^2\mathrm{d}\hat{s}$$

$$\varepsilon\lambda_3 = \frac{v_0^2 gB\cos\alpha}{2EI\omega_0^2}\int_0^1 \Psi'^4\mathrm{d}\hat{s}$$

$$\varepsilon\beta = \frac{v_0^2}{l^2}\left(\int_0^1 \Psi\Psi''\int_1^{\hat{s}}\int_0^{\hat{s}_2}\Psi'^2\mathrm{d}\hat{s}_1\mathrm{d}\hat{s}_2\mathrm{d}\hat{s} + \int_0^1 \Psi\Psi'\int_0^{\hat{s}}\Psi'^2\mathrm{d}\hat{s}_1\mathrm{d}\hat{s}\right)$$

$$\varepsilon\eta_1 = \frac{gBl^3\sin\alpha}{EIv_0\omega_0^2}\Psi|_{\hat{s}=1}$$

the slow-flow equations are given by:

$$\begin{aligned} a' &= -\frac{\varepsilon}{2}\left[\frac{a}{Q} + i_0\eta_1\sin(\phi - \varepsilon\sigma\tau)\right] + O(\varepsilon^2), \\ a\phi' &= \frac{\varepsilon}{8}\left[(3k_3 - 2\beta)a^3 - 4i_0\eta_1\cos(\phi - \varepsilon\sigma\tau)\right] + O(\varepsilon^2). \end{aligned} \tag{10}$$

To further simplify the slow-flow equations, two additional coordinate transformations of $\hat{\tau} = \varepsilon\tau$ and $\theta = \phi - \varepsilon\sigma\tau$ can be introduced. This yields,

$$\begin{aligned} a' &= -\frac{1}{2}\left[\frac{a}{Q} + i_0\eta_1\sin\theta\right], \\ a\theta' &= \frac{1}{8}\left[(3k_3 - 2\beta)a^3 - 4i_0\eta_1\cos\theta - 8\sigma a\right]. \end{aligned} \tag{11}$$

Note that in Eqn. (11), implicitly

$$(\bullet)' = \frac{\partial(\bullet)}{\partial\hat{\tau}} \tag{12}$$

and that a and θ are functions of $\hat{\tau}$. By solving for the steady-state solutions of Eqn. (11), a third-order polynomial equation that relates the displacement amplitude to the excitation frequency can be derived

$$16Q^2 i_0^2\eta_1^2 = A\left[16 + Q^2(\alpha_3 A - 8\sigma)^2\right], \tag{13}$$

where $\alpha_3 = 3k_3 - 2\beta$ and $a^2 = A$. From this equation, it can be seen that the maximum amplitude is given by $i_0\eta_1 Q$, and it occurs at $\sigma = \alpha_3 i_0^2\eta_1^2 Q^2/8$. The threshold value of current corresponding to the onset of bistability (i_{cr}) can be calculated by invoking the implicit function theorem:

$$i_{cr} = \frac{4\sqrt{2}}{3^{3/4}Q^{3/2}\sqrt{|\alpha_3|}\eta_1}. \tag{14}$$

Note that below this critical value the response is single valued and stable, and above the critical current there exists a finite range of frequency where multiple steady-state solutions exist [17].

Using Eqn. (13), the frequency response characteristics of the system can be investigated. Figure 4 depicts the velocity of the resonator as a function of the excitation frequency, for a representative device with parameters given as shown in Table 2. Here, the stable steady-state solutions are represented by solid lines, while unstable solutions are denoted by dashed lines. Note that the quality factor employed here was selected to match experimental values obtained from frequency sweeps conducted within the linear response regime. Also note that the value for the total resistance of the device utilized here accounts for the resistance of the Au/Cr wires and the coaxial cables used to interface with the device. Finally, note that the observed behavior is consistent with the Duffing-like response structure predicted by Eqn. (13).

3 THE INDUCED ELECTROMOTIVE FORCE

As noted earlier, the vibration of the microcantilever in a permanent magnetic field results in an induced EMF. As previously noted in [16], the induced EMF due to mechanical vibrations (V_{emf}) is approximated to third-order by

$$V_{emf} = \kappa_1 z' + \kappa_2 z z', \tag{15}$$

where

$$\begin{aligned} \kappa_1 &= -\frac{Bg\sin\alpha v_0\omega_0}{T}\frac{\int_0^1\Psi\int_0^1\Psi'\mathrm{d}\hat{s}\mathrm{d}\hat{s}}{\int_0^1\Psi\mathrm{d}\hat{s}}, \\ \kappa_2 &= \frac{Bg\cos\alpha v_0^2\omega_0}{lT}\frac{\int_0^1\Psi\int_0^1\Psi'^2\mathrm{d}\hat{s}\mathrm{d}\hat{s}}{\int_0^1\Psi\mathrm{d}\hat{s}}. \end{aligned} \tag{16}$$

TABLE 2. DIMENSIONS AND MATERIAL PROPERTIES USED TO STUDY THE DYNAMIC RESPONSE OF A REPRESENTATIVE ELECTROMAGNETICALLY-ACTUATED MICROCANTILEVER. BASED ON THESE VALUES, THE NATURAL FREQUENCY IS EXPECTED TO BE APPROXIMATELY 29.65 kHZ. THE QUALITY FACTOR WAS CHOSEN TO MATCH THE EXPERIMENTAL VALUES OBTAINED FROM FREQUENCY SWEEPS CONDUCTED WITHIN IN THE LINEAR RESPONSE REGIME.

Physical Parameter	Value
Length of Beam (l)	300 μm
Width (g)	50 μm
Thickness (v_0)	2 μm
Young's Modulus (E)	159 GPa
Mass Density (ρ)	2330 kg/m^3
Magnetic Field Strength (B)	1 T
Magnetic Field Orientation (α)	$\pi/3$ rad
Au/Cr Trace Resistance ($R_{Au/Cr}$)	30 Ω
Quality Factor (Q)	6800

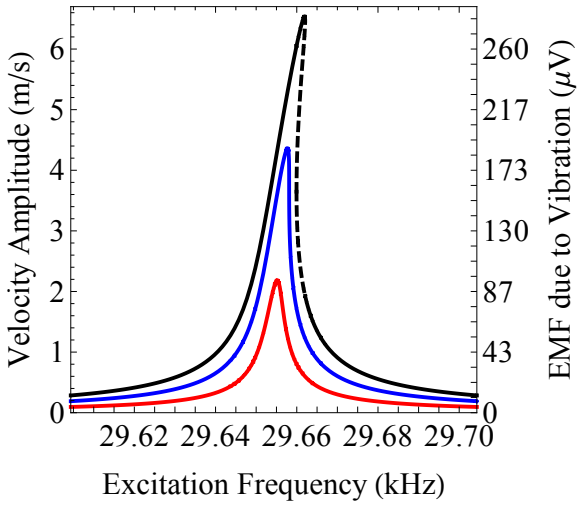

FIGURE 4. STEADY-STATE VELOCITY AMPLITUDE PLOTTED AS A FUNCTION OF THE EXCITATION FREQUENCY FOR A DEVICE WITH DIMENSIONS AND MATERIAL PROPERTIES GIVEN AS SHOWN IN TABLE 2. NOTE THAT IN THIS FIGURE, AND IN FIGS. 6-9, THE RESPONSES SHOWN IN RED, BLUE AND BLACK CORRESPOND TO EXCITATION VOLTAGES OF 1.93 mV, 3.85 mV AND 5.78 mV, RESPECTIVELY. THE RESPONSE SHOWN IN BLUE CORRESPONDS TO THE ONSET OF BISTABILITY.

An equivalent circuit, which describes the electrical coupling between the input and output of this device, is shown in Fig. 5. The voltage applied to the device is defined as V_{in}. This excitation supplies a current through a coaxial cable of resistance R_{Co}, which is henceforth assumed to be 50 Ω. This current is then split into two components $i(\tau)$ and i_d, where $i(\tau)$ is the current in the outer Au/Cr wire trace and i_d is the current in the inner Au/Cr wire trace. Each of these wire traces are modeled as resistors, with resistance $R_{Au/Cr}$, and inductors, with self-inductance L and mutual inductance M, in series. To account for the induced EMF produced by the vibration of the microcantilever, a voltage source that is controlled by the current in the outer wire is included in the branch that models the inner wire. Note that since the EMF due to mechanical vibration is small in comparison to the actuation voltage, a second current controlled voltage source is not accounted for in the branch that models the outer wire loop. The resistive coupling between the input and output is accounted for with R_{Si}, which is the lumped resistance due to the conduction between the inner and outer wires. Finally, V_m is the measured voltage.

To develop a simplified model for the measured voltage, it is assumed that the inductances are very small and that R_{Si} is very large. Note that experimentally R_{Si} has been measured to be greater than 1 MΩ. Accordingly, the current supplied to the outer wire is approximately

$$i(\tau) = \frac{V_{in}}{R_{Au/Cr} + R_{Co}}. \tag{17}$$

Note that under these assumptions, $V_1 = i(\tau)R_{Au/Cr}$. By applying Kirchhoff's current law to the node where V_m is present and using the fundamental relationship between the current and voltage for an inductor, under the assumption that $i(\tau) >> i_d$, two equations, which can be used to solve for the measured voltage, are generated:

$$\begin{aligned} \frac{V_1 - V_m}{R_{Si}} &= \frac{V_m - V_2}{R_{Au/Cr}}, \\ V_2 - V_{EMF} &= -M\frac{\omega_0}{T} i'(\tau). \end{aligned} \tag{18}$$

These equations reveal that, under the stated assumptions, the measured voltage is effectively the superposition of three effects: the induced EMF due to the vibration of the microcantilever, the inductive coupling between the wire loops and the resistive cou-

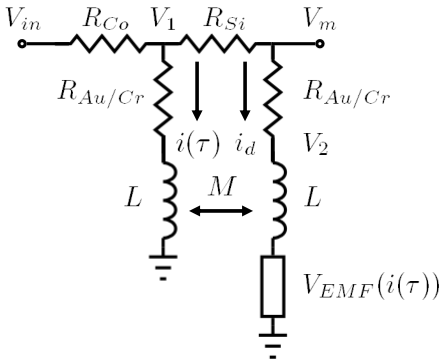

FIGURE 5. EQUIVALENT CIRCUIT DIAGRAM USED TO MODEL THE ELECTRICAL COUPLING BETWEEN THE INPUT AND OUTPUT PORTS OF THE PRESENTED DEVICE. AN EXCITATION SIGNAL IS PROVIDED BY A VOLTAGE SOURCE V_{in}, WHICH SUPPLIES A CURRENT THROUGH A COAXIAL CABLE OF RESISTANCE R_{Co}. THE INNER AND OUTER WIRE LOOPS ARE MODELED AS RESISTORS $R_{Au/Cr}$ AND INDUCTORS IN SERIES, WITH SELF-INDUCTANCE L AND MUTUAL INDUCTANCE M. THE CURRENTS IN THE OUTER AND INNER LOOPS ARE DEFINED AS $i(\tau)$ AND i_d, RESPECTIVELY. THESE WIRE LOOPS ARE ISOLATED BY A RESISTOR R_{Si}, WHICH MODELS THE CONDUCTION BETWEEN THE TWO LOOPS. TO CAPTURE THE EFFECTS OF THE EMF INDUCED BY MECHANICAL VIBRATION, A CURRENT-CONTROLLED VOLTAGE SOURCE IS ADDED IN SERIES WITHIN THE BRANCH THAT REPRESENTS THE INNER WIRE LOOP. NOTE THAT R_{Si} IS ASSUMED TO BE VERY LARGE, SUCH THAT $i(\tau) >> i_d$, AND THE INDUCTANCES L AND M ARE VERY SMALL.

pling due to conduction in the silicon of the microcantilever:

$$V_m = c_1 V_{EMF}[i(\tau)] + c_2 i(\tau) - c_3 i'(\tau), \tag{19}$$

where

$$\begin{aligned} c_1 &= \frac{R_{Si}}{R_{Si}+R_{Au/Cr}}, \\ c_2 &= \frac{R_{Au/Cr}^2}{R_{Si}+R_{Au/Cr}}, \\ c_3 &= \frac{M\omega_0 R_{Si}}{T(R_{Si}+R_{Au/Cr})}. \end{aligned} \tag{20}$$

Note that for physically-consistent systems, c_1 is approximately one, c_2 is nearly zero and c_3 is the mutual inductance, scaled to account for the nondimensionalized time.

Since the EMF is measured in experiments using a lock-in amplifier that is set to measure at the excitation frequency, higher order harmonics in the induced EMF due to vibration are filtered out. Thus, using the results from above,

$$V_m = -c_1\kappa_1 a\sin(\Omega\tau+\theta) + c_2 i_0\cos(\Omega\tau) + c_3 i_0\sin(\Omega\tau). \tag{21}$$

Equation (21) can be rewritten such that the amplitude and phase of the measured EMF can be easily identified:

$$\begin{aligned} V_m &= a_m\cos[\Omega\tau+\theta_m], \\ a_m &= \sqrt{\left(c_2 i_0 + \frac{c_1\kappa_1 A}{i_0 Q\eta_1}\right)^2 + \left(\frac{c_1\kappa_1 A(A\alpha_3-8\sigma)}{4i_0\eta_1} - c_3 i_0\right)^2}, \\ \tan[\theta_m] &= \frac{Q\left(c_1\kappa_1 A\left(A\alpha_3-8\sigma\right) - 4c_3\eta_1 i_0^2\right)}{4\left(c_1\kappa_1 A + c_2\eta_1 Q i_0^2\right)}. \end{aligned} \tag{22}$$

When the quality factor is large and the effects of resistive coupling are small, the first term in a_m can be ignored. Since the values in the second term are of opposite sign, it is possible that this term can equal zero, thus when inductive coupling is dominant, an *effective antiresonance* can be created. In addition, the equation for a_m predicts that the magnitude of the input current i_0 biases the response such that nonresonant responses are nontrivial and are scaled in an approximately linear fashion by i_0.

Figures 6-9 depict the amplitude of the measured EMF for the same excitation levels used in Fig. 4, with different values of the mutual inductance M and the silicon substrate resistance R_{Si}. The same convention for classifying the excitation levels and stability used in Fig. 4 are employed. For the case shown in Fig. 6, where the effects of mutual inductance and resistive coupling are small, the amplitude response is very similar to those depicted in Fig. 4. When just the mutual inductance is increased, as shown in Fig. 7, the response is warped such that an *effective antiresonance* is created and the nonresonant responses are scaled with the excitation level. If just the resistive coupling is increased, as shown in Fig. 8, a response bias is observed. If both the inductive coupling and resistive coupling are increased, as shown in Fig. 9, then not only are both effects observed, but they are also exaggerated.

Clearly, from the results presented here, input/output coupling significantly alters both the qualitative and quantitative nature of the measurable EMF signal, and thus must be accounted for in the course of predictive design. It is also important to note that due to the coupling between the input and output ports, broadband noise in the input can significantly degrade the signal to noise ratio associated with the device. Likewise, since the amplitude of the frequency response is nontrivial away from resonance, excitations at those frequencies are not filtered from the response.

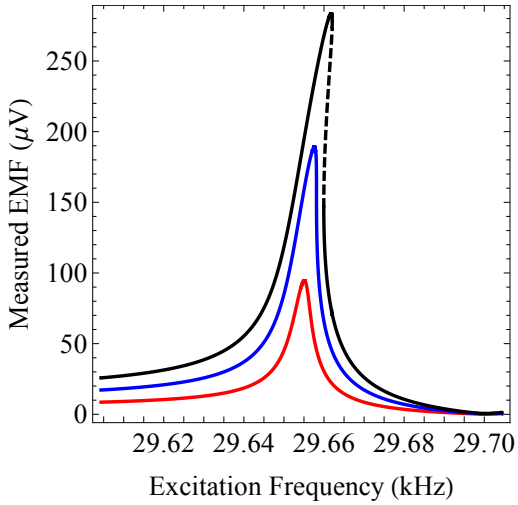

FIGURE 6. ANALYTICALLY-PREDICTED MEASURED EMF PLOTTED AS A FUNCTION OF THE EXCITATION FREQUENCY FOR A LOW INPUT COUPLING CASE WHERE $R_{Si} = 2$ MΩ AND $M = 1$ μH. THIS RESPONSE IS VERY SIMILAR TO THE ONE DEPICTED IN FIG. 4, BUT AN ANTIRESONANCE AND RESPONSE BIAS ARE OBSERVED.

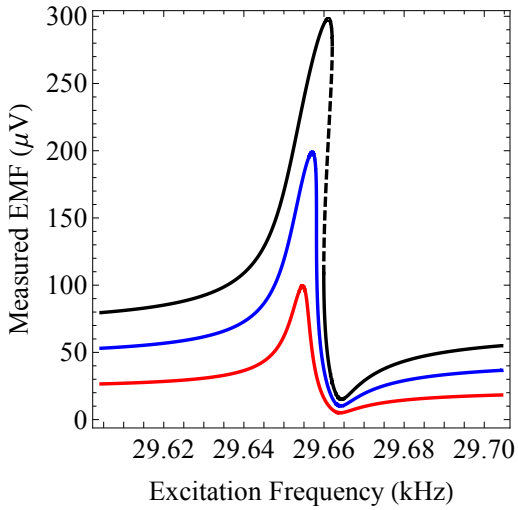

FIGURE 7. ANALYTICALLY-PREDICTED MEASURED EMF PLOTTED AS A FUNCTION OF THE EXCITATION FREQUENCY FOR A HIGH INDUCTIVE COUPLING CASE WHERE $R_{Si} = 2$ MΩ and $M = 5$ μH. IN THIS RESPONSE AN EFFECTIVE ANTIRESONANCE IS READILY APPARENT.

4 EXPERIMENTAL RESULTS

To validate the results presented in the previous section, a series of devices were fabricated at the Birck Nanotechnology Center using standard silicon-on-insulator (SOI) microfabrication processes (see Fig. 10). The process used an SOI wafer, 4

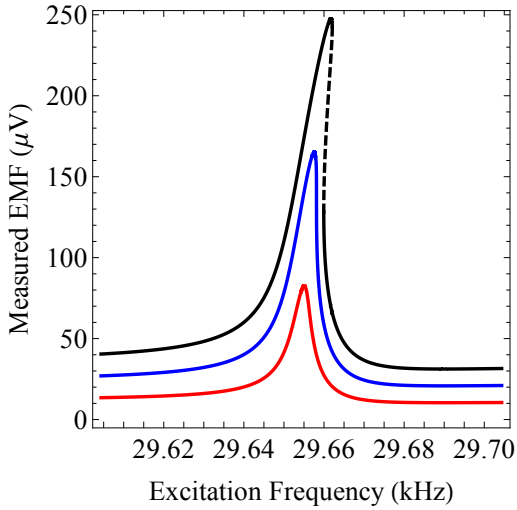

FIGURE 8. ANALYTICALLY-PREDICTED MEASURED EMF PLOTTED AS A FUNCTION OF THE EXCITATION FREQUENCY FOR A HIGH RESISTIVE COUPLING CASE WHERE $R_{Si} = 2$ kΩ and $M = 1$ μH. WHILE AN ANTIRESONANCE IS NOT APPARENT, A RESPONSE BIAS IS PROMINENT.

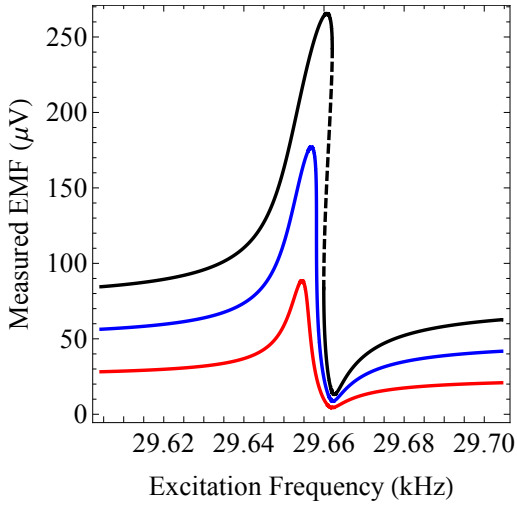

FIGURE 9. ANALYTICALLY-PREDICTED MEASURED EMF PLOTTED AS A FUNCTION OF THE EXCITATION FREQUENCY FOR A HIGH INPUT COUPLING CASE WHERE $R_{Si} = 2$ kΩ and $M = 5$ μH. BOTH THE ANTIRESONANCE AND BIAS EFFECT ARE READILY APPARENT IN THE RESPONSE.

inches in diameter. The device layer was p-type doped silicon with very high resistivity ($>1000\ \Omega - \text{cm}$) and was 2 μm thick, the oxide layer was 2 μm thick and the handle layer was 500 μm thick. Wire loops were formed by evaporating Cr and Au on the surface and then using a lift-off process. The cantilevers were formed using reactive ion etching on the device layer. The oxide

layer was exposed using deep reactive ion etching on the handle layer and then the devices were released using hydrofluoric acid.

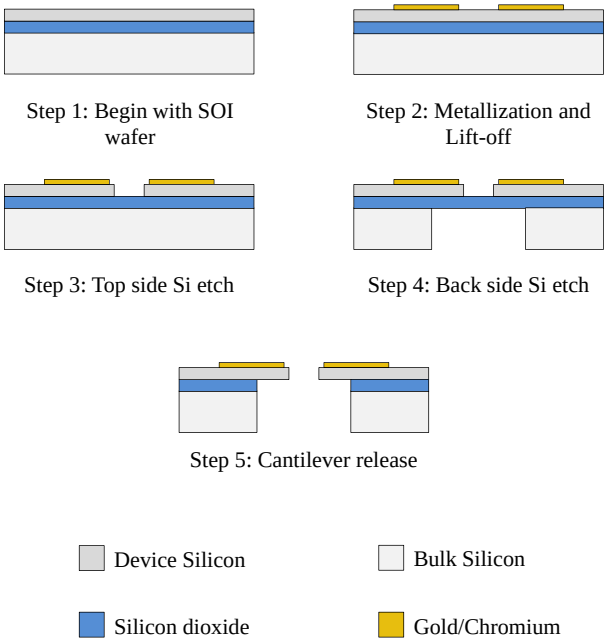

FIGURE 10. FABRICATION PROCESS FLOW USED TO PRODUCE THE ELECTROMAGNETICALLY-TRANSDUCED MICRORESONATORS.

To experimentally characterize the response of these devices, a Polytec MSA-400 laser Doppler vibrometer (LDV) was used in conjunction with a SUSS MicroTec PLV-50 vacuum probe station. Figure 11 shows a part of the experimental setup used to study the optical response. The probe station consists of a vacuum chamber, whose pressure is controllable to a minimum set point of 75 μTorr. The devices are placed in a permanent magnetic field with a field strength of approximately 1 T near the poles. The permanent magnet used for these experiments is a NdFeB slab magnet with dimensions 1" x 1" x 0.1".

The device was placed in the probe station at a pressure setting of 75 μTorr and the device was positioned on the magnet such that the fixed edge of the microcantilever is on the edge of the magnet. The quality factor for these devices was 6840. The combined resistance of the outer Au/Cr trace with the coaxial cable was 65 Ω, while the same measurement for the inner loop was approximately 70 Ω. The input waveform was generated using an Agilent 33250A arbitrary waveform generator and the response was measured using an SR844 lock-in amplifier. Figure 12 shows the block diagram of the experimental setup used to perform these electrical measurements. The devices were actu-

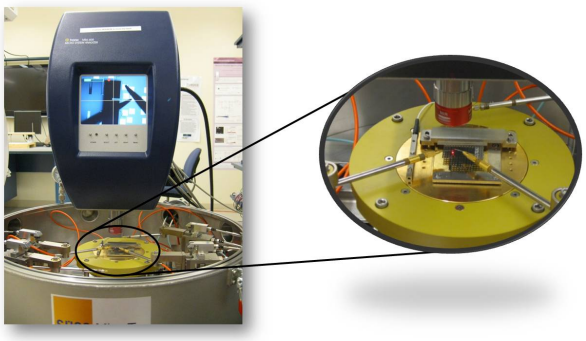

FIGURE 11. A PART OF THE EXPERIMENTAL SETUP USED TO CHARACTERIZE THE DYNAMIC RESPONSE OF THE ELECTROMAGNETICALLY-TRANSDUCED MICRORESONATORS. A POLYTEC MSA-400 LASER DOPPLER VIBROMETER WAS USED IN CONJUNCTION WITH A SUSS MICROTEC PLV50 PROBE STATION FOR THIS PURPOSE. THE DEVICES WERE PLACED IN A PERMANENT MAGNETIC FIELD, IN THE CHAMBER WITH A PRESSURE OF 75 μTorr.

ated using the outer current loop. To perform the electrical measurements, the induced EMF from the inner loop was measured using the lock-in amplifier, while for the optical measurements, the output from the LDV was measured using the lock-in amplifier.

As can be extrapolated from the discussion presented in Section 3, noise in the input can render significant noise in the output. Primarily due to the inductive coupling between the input and output, high frequency components of noise from the source are not filtered from the response. If the measurement was devoid of noise, the time constant used for the lock-in would be set to filter the response at twice the excitation frequency, which is produced from signal mixing in the lock-in. Based on the excitation frequencies used, this time constant would be on the order of less than a millisecond. Nominally, the spurious output of the 33250A is -70 dBc with a noise bandwidth of 10 MHz. Thus, to get an estimate for the amplitude with a small standard deviation, a much larger time constant of 1 second was used. Since a 12 dB/oct filter slope was used, the recommend dwell time is 7 time constants, to ensure that the measurement settles to within 99% of its final value. Since a large time constant was used, to decrease the time required for a single trial the dwell time was reduced to 1 second, effectively windowing the response with a moving average filter. Thus, the included experimental responses are not *exactly* the same type of measurement as shown in the previous section, but the two responses are very strongly correlated.

Figure 13 depicts representative experimentally-recovered responses, obtained optically from the LDV and electrically from the measured EMF, for an excitation level of 10 mVpp. It is ev-

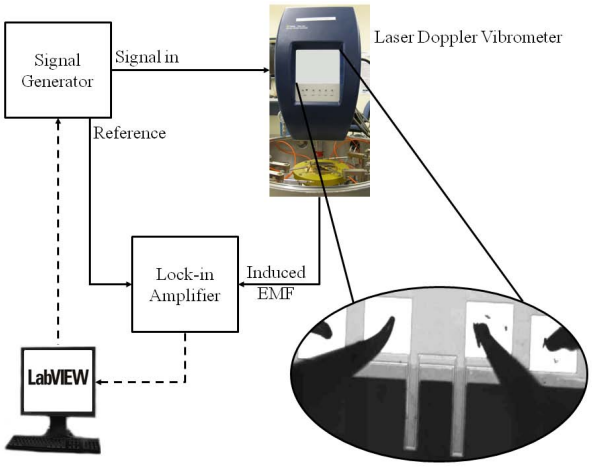

FIGURE 12. BLOCK DIAGRAM OF THE ELECTRICAL SETUP USED TO PERFORM ELECTRICAL MEASUREMENTS ON THE ELECTROMAGNETICALLY-TRANSDUCED MICRORESONATORS.

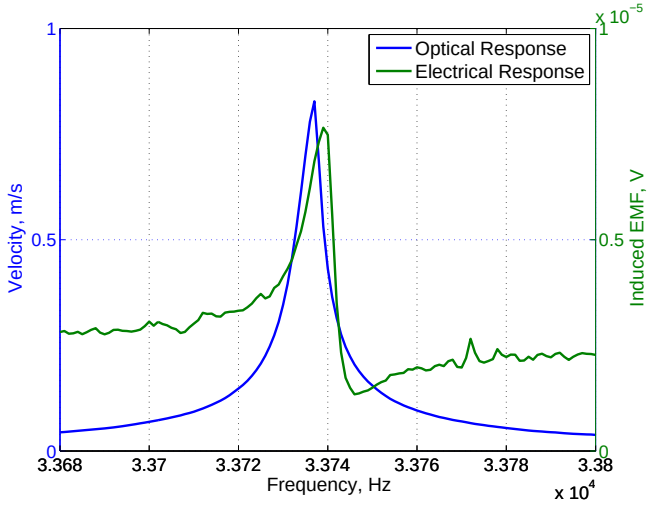

FIGURE 13. EXPERIMENTALLY-RECOVERED FREQUENCY RESPONSES FROM OPTICAL AND ELECTRICAL MEASUREMENTS, FOR AN EXCITATION LEVEL OF 10 mVpp. THE ELECTRICAL RESPONSE CORRELATES WELL WITH THE OPTICAL RESPONSE WITH RESPECT TO THE NATURAL FREQUENCY, AND QUALITATIVELY MATCHES THE RESPONSE PREDICTED BY THE MODEL.

ident that the measured electrical response correlates well with the optical response in terms of the natural frequency. However, the recovered electrical response demonstrates effects related to resistive and inductive coupling, such as a nontrivial response away from resonance and the presence of an effective antiresonance.

Figure 14 shows the experimentally-recovered electrical responses as a function of excitation amplitude. The amplitude response clearly shows that the resonator vibrates with a higher velocity as the excitation amplitude increases. The plot also reveals that the response becomes increasingly nonlinear with increasing excitation amplitude. This is consistent with behavior predicted by the model developed in the previous section.

In order to study the nonlinear behavior of these resonators, frequency sweeps were performed near the first natural frequency. Both forward (increasing frequency) and reverse (decreasing frequency) sweeps were performed. Figure 15 shows the result of the sweeps performed at an excitation level of 50 mVpp. The amplitude responses show distinct nonlinear behavior and distinct hysteresis with respect to the excitation frequency.

5 CONCLUSIONS AND FUTURE DIRECTIONS

In this work, a model to describe the dynamics of an electrically- and mechanically-isolated electromagnetically-actuated microcantilever has been developed. The model accounts for the intrinsic coupling between the device's input and output ports, which introduce additional features in the response. Specifically, the electrical effects introduce an antiresonance and a bias, which significantly alter the dynamics of the device. Experimental results recovered from SOI-based devices validate that the model qualitatively captures the behavior of the device. Current and future research efforts include redesigning the wire loops so as to mitigate or exploit the effects of coupling and noise, and demonstrating the utility of these devices in signal processing applications.

ACKNOWLEDGEMENTS

This material is based in part upon work supported by the National Science Foundation under Grant Number 0846385. Any opinions, findings, and conclusions or recommendations expressed in this material are those of the authors and do not necessarily reflect the views of the National Science Foundation.

REFERENCES

[1] Ekinci, K. L., Huang, X. M. H., and Roukes, M. L., 2004. "Ultrasensitive nanoelectromechanical mass detection". *Applied Physics Letters,* ***84***(22), pp. 4469–4471.

[2] Greywall, D. S., Yurke, B., Busch, P. A., Pargellis, A. N., and Willett, R. L., 1994. "Evading amplifier noise in nonlinear oscillators". *Physical Review Letters,* ***72***(19), pp. 2992–2995.

[3] Greywall, D. S., 1999. "Micromechanical RF filters excited by the Lorentz force". *Journal of Micromechanics and Microengineering,* ***9***(1), pp. 78–84.

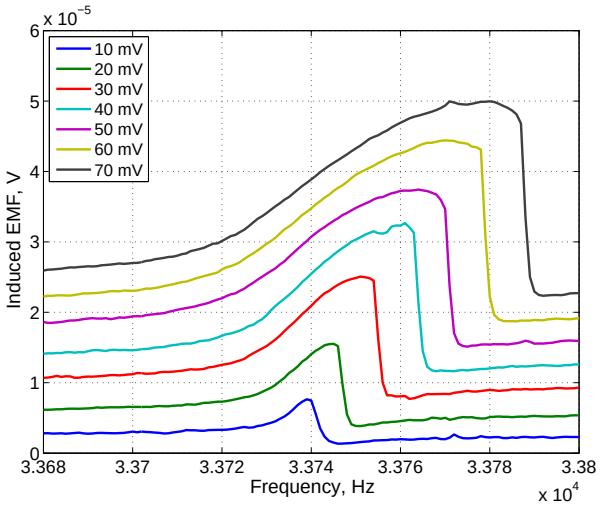

FIGURE 14. EXPERIMENTALLY-RECOVERED AMPLITUDE RESPONSE FROM ELECTRICAL MEASUREMENTS FOR VARYING EXCITATION LEVELS. THE RESPONSES CLEARLY SHOW THAT THE RESONATOR VIBRATES WITH A HIGHER AMPLITUDE AS THE EXCITATION AMPLITUDE INCREASES. THE RESPONSE ALSO BECOMES INCREASINGLY NONLINEAR WITH INCREASING EXCITATION AMPLITUDE.

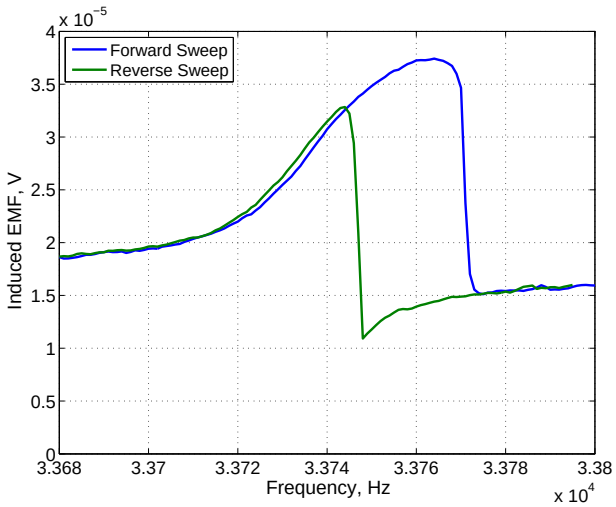

FIGURE 15. EXPERIMENTALLY-RECOVERED AMPLITUDE RESPONSE FROM THE ELECTRICAL MEASUREMENTS, DURING FORWARD AND REVERSE SWEEPS AT AN EXCITATION LEVEL OF 50 mVpp. THE RESPONSE SHOWS A CLEAR NONLINEAR BEHAVIOR AND A HYSTERESIS IN THE RESPONSE BETWEEN THE FORWARD AND THE REVERSE SWEEPS.

[4] Martin, S. J., Butler, M. A., Spates, J. J., Mitchell, M. A., and Schubert, W. K., 1998. "Flexural plate wave resonator excited with Lorentz forces". *Journal of Applied Physics,* ***83***(9), pp. 4589–4601.

[5] Schiffer, M., Laible, V., and Obermeier, E., 2002. "Design and fabrication of 2D Lorentz force actuated micromirrors". In the Proceedings of the 2002 IEEE/LEOS International Conference on Optical MEMS, pp. 163–164.

[6] Jun, S. C., Huang, X. M. H., Hone, J., Zorman, C. A., and Mehregany, M., 2005. "Evaluation of 3C-SiC nanomechanical resonators using room temperature magnetomotive transduction". In the Proceedings of IEEE Sensors 2005: The 4th IEEE Conference on Sensors, pp. 1042–1045.

[7] Huang, X. M. H., Feng, X. L., Zorman, C. A., Mehregany, M., and Roukes, M. L., 2005. "VHF, UHF and microwave frequency nanomechanical resonators". *New Journal of Physics,* ***7***(247), pp. 1–15.

[8] Thompson, M. J., and Horsley, D. A., 2011. "Parametrically amplified z-axis Lorentz force magnetometer". *Journal of Microelectromechanical Systems,* ***20***(3), pp. 702–710.

[9] Requa, M. V., and Turner, K. L., 2006. "Electromechanically driven and sensed parametric resonance in silicon microcantilevers". *Applied Physics Letters,* ***88***(26), p. 263508.

[10] Requa, M. V., 2006. "Parametric resonance in microcantilevers for applications in mass sensing". Ph.D. Dissertation. University of California, Santa Barbara. Santa Barbara, California.

[11] Requa, M. V., and Turner, K. L., 2007. "Precise frequency estimation in a microelectromechanical parametric resonator". *Applied Physics Letters,* ***90***(17), p. 173508.

[12] Rhoads, J. F., 2007. "Exploring and exploiting resonance in coupled and/or nonlinear microelectromechanical oscillators". Ph.D. Dissertation. Michigan State University. East Lansing, Michigan.

[13] Kumar, V., Sabater, A., and Rhoads, J. F., 2011. "Dynamics of coupled electromagnetically-actuated microbeams". In the Proceedings of the 2011 NSF Engineering Research and Innovation Conference.

[14] Sazonova, V., Yaish, Y., Ustunel, H., Roundy, D., Arias, T. A., and McEuen, P. L., 2004. "A tunable carbon nanotube electromechanical oscillator". *Nature,* ***431***(7006), pp. 284–287.

[15] Lassagne, B., Garcia-Sanchez, D., Aguasca, A., and Bachtold, A., 2008. "Ultrasensitive mass sensing with a nanotube electromechanical resonator". *Nano Letters,* ***8***(11), pp. 3735–3738.

[16] Sabater, A. B., and Rhoads, J. F., 2012. "On the dynamics of two mutually-coupled, electromagnetically-actuated microbeam oscillators". *Journal of Computational and Nonlinear Dynamics, to appear*.

[17] Nayfeh, A. H., and Mook, D. T., 1995. *Nonlinear Oscillations*. Wiley-Interscience.